A&A 472, 587–598 (2007)
DOI: 10.1051/0004-6361:20067015

Astronomy & Astrophysics

Multiwavelength optical observations of chromospherically active binary systems

V. FF UMa (2RE J0933+624): a system with orbital period variation[⋆],[⋆⋆]

M. C. Gálvez[1,2], D. Montes[1], M. J. Fernández-Figueroa[1], E. De Castro[1], and M. Cornide[1]

[1] Departamento de Astrofísica, Facultad de Ciencias Físicas, Universidad Complutense de Madrid, 28040 Madrid, Spain
e-mail: `mcz@astrax.fis.ucm.es`
[2] Department of Astronomy, University of Florida, Gainesville, FL 32611, USA

Received 22 December 2006 / Accepted 31 May 2007

ABSTRACT

Context. This is the fifth paper in a series aimed at studying the chromospheres of active binary systems using several optical spectroscopic indicators to obtain or improve orbital solution and fundamental stellar parameters.

Aims. We present here the study of FF UMa (2RE J0933+624), a recently discovered, X-ray/EUV selected, active binary with strong Hα emission. The objectives of this work are, to find orbital solutions and define stellar parameters from precise radial velocities and carry out an extensive study of the optical indicators of chromospheric activity.

Methods. We obtained high resolution echelle spectroscopic observations during five observing runs from 1998 to 2004. We found radial velocities by cross correlation with radial velocity standard stars to achieve the best orbital solution. We also measured rotational velocity by cross-correlation techniques and have studied the kinematic by galactic space-velocity components (U, V, W) and Eggen criteria. Finally, we have determined the chromospheric contribution in optical spectroscopic indicators, from Ca II H & K to Ca II IRT lines, using the spectral subtraction technique.

Results. We have found that this system presents an orbital period variation, higher than previously detected in other RS CVn systems. We determined an improved orbital solution, finding a circular orbit with a period of 3.274 days. We derived the stellar parameters, confirming the subgiant nature of the primary component ($M_{\rm P} = 1.67\ M_{\odot}$ and $R \sin i_{\rm P} = 2.17\ R_{\odot}$) and obtained rotational velocities ($v \sin i$), of 33.57 ± 0.45 km s^{-1} and 32.38 ± 0.75 km s^{-1} for the primary and secondary components respectively. From our kinematic study, we can deduce its membership to the Castor moving group. Finally, the activity study has given us a better understanding of the possible mechanisms that produce the orbital period variation.

Key words. stars: activity – stars: binaries: spectroscopic – stars: chromospheres – stars: late-type

1. Introduction

This paper is a continuation of our ongoing project aimed at studying the chromospheres of active binary systems using multiwavelength optical observations. These observations provide the information for several optical spectroscopic features that are formed at different heights in the chromosphere (see Montes et al. 1997, Paper I; Montes et al. 1998, Paper II; Montes et al. 2000, Paper III; Gálvez et al. 2002, Paper IV). In addition to studying stellar activity, our high resolution spectroscopic observations allow us to determine radial velocities and obtain and improve fundamental stellar parameters. While several systems have been studied, this is the first time we have found an orbital period variation, giving us new clues into the understanding of activity-orbit relation. When combined with other examples, the study of this type of system could help us understand how orbital dynamics are affected by physical processes intrinsic to the binary system (Lanza 2006).

We focus here on the X-ray/EUV selected chromospherically active binary FF UMa (2RE J0933+624, HD 82286, SAO 14919). It is an SB2 system with $V = 8.35$ mag. First classified by Jeffries et al. (1995) as two G5V or G5V/G5IV stars, it was reclassified by Henry et al. (1995) and Strassmeier et al. (2000) as an K0IV/K0IV.

Henry et al. (1995) reported a photometric period of 3.270 days obtained from a periodogram analysis derived from photometric data, and estimated a rotational velocity $v \sin i = 35$ km s^{-1} for both components. Jeffries et al. (1995) obtained an orbital period of 3.28 days from 15 radial velocity measurements and suggested an eccentricity less than 0.18. Their estimated value of $R \sin i$ was in agreement with a subgiant primary. Strassmeier et al. (2000) found a rotational period of 3.207 days and photometric variation amplitudes of $\Delta V \approx 0.15$ mag. All previous authors have reported that this star presents very strong

---

[⋆] Based on observations collected with the 2.2 m telescope at the Centro Astronómico Hispano Alemán (CAHA) at Calar Alto (Almería, Spain), operated jointly by the Max-Planck Institut für Astronomie and the Instituto de Astrofísica de Andalucía (CSIC); with the Nordic Optical Telescope (NOT), operated on the island of La Palma jointly by Denmark, Finland, Iceland, Norway and Sweden, in the Spanish Observatorio del Roque de Los Muchachos of the Instituto de Astrofísica de Canarias; with the 2.1 m Otto Struve Telescope at McDonald Observatory of the University of Texas at Austin (USA) and with Hobby-Eberly Telescope, which is a joint project of the University of Texas at Austin, the Pennsylvania State University, Stanford University, Ludwig-Maximilians-Universität München, and Georg-August-Universität Göttingen.

[⋆⋆] Tables 7 and 8 are only available in electronic form at `http://www.aanda.org`

Table 1. Observing log.

2.1 m-Sandiford 1998/01			9.2 m McDonald 2000/01			2.2 m-FOCES 2002/04			2.2 m-FOCES 2004/04			NOT-SOFIN 2004/04		
Day	UT	S/N (Hα)	Day	UT	S/N (Hα)	Day	UT	S/N (Hα)	Day	UT	S/N (Hα)	Day	UT	S/N (Hα)
13	10:27	146	19	06:12	233	22	19:54	118	31	23:36	71	2	21:53	225
14	9:58	203	23	06:34	263	23	19:41	200	2	19:38	63	2	22:02	180
15	10:07	98	24	07:29	83	24	19:45	140	3	19:23	87	4	00:56	243
16	10:19	139	25	06:24	146	25	21:55	146	3	23:22	74	5	21:33	227
17	10:23	95	26	10:12	236				4	02:46	59			
18	11:04	134							4	19:18	95			
19	11:00	146							4	22:23	117			
20	10:27	83							5	01:43	80			
21	10:52	77							5	19:23	56			
22	12:57	115							5	22:29	122			
									6	02:14	130			
									6	19:20	117			
									7	01:32	93			

chromospheric activity and the Hα emission line is detected above the continuum for both components.

In this paper, we present high-resolution echelle spectra of this system. We measured radial velocities using the cross-correlation technique and obtained an orbital period variation during 11 years of observations. In spite of this variation, we achieved a good orbital solution, finding that the mean orbital period is similar to the photometric one, indicating synchronous rotation.

In addition, we applied the spectral subtraction technique to study the chromospheric excess emission in the Ca II H & K, Ca II IRT, Hα and other Balmer lines of the primary and secondary components of the system. Preliminary results for this system can be found in Gálvez (2005); and Gálvez et al. (2006, 2007).

In Sect. 2 we give the details of our observations and data reduction. In Sect. 3 we discuss the nature of the orbital period variation and give the orbital solution of the binary system. In Sect. 4 we give the derived stellar and kinematic parameters. The behavior of the different chromospheric activity indicators is described in Sect. 5. Finally, in Sect. 6 we present our conclusions.

2. Observations and data reduction

We obtained high resolution echelle spectra of FF UMa during five observing runs from 1998 to 2004:

1) 2.1 m-SANDIFORD, McDonald Obs., 1998/01.
During this observing run, which extended from 12 to 21 January 1998, we used the 2.1 m Otto Struve Telescope at McDonald Observatory Texas (USA) with the Sandiford Cassegrain Echelle Spectrometer (SCES), equipped with a 1200 × 400 pixel CCD detector. The wavelength range covers from 6400 to 8800 Å in 31 orders. The reciprocal dispersion ranges from 0.06 to 0.08 Å/pixel and the spectral resolution, determined as the full width at half maximum (*FWHM*) of the arc comparison lines, from 0.13 to 0.20 Å. In the fourth night, the central wavelength was changed to include the Na I D_1, D_2 (5889.95, 5895.92 Å) and He I D_3 (5876 Å) lines. Therefore the wavelength range changed to 5600–7000 Å.

2) 9.2 m-HET, McDonald Obs., 2000/01.
We used the 9.2 m Hobby-Eberly Telescope (HET) and the medium resolution spectrograph UFOE (Upgraded Fiber Optic Echelle) equipped with a 1200×400 pixel CCD detector, located at McDonald Observatory Texas (USA) on 22 to 24 January 2000. The wavelength range covers from 4400 to 9150 Å in 26 orders. The reciprocal dispersion ranges from 0.06 to 0.17 Å/pixel and the spectral resolution (*FWHM*) ranges from 0.14 to 0.42 Å.

3) and 4) 2.2 m-FOCES, CAHA, 2002/04 and 2004/04.
We utilized the Fibre Optics Cassegrain Echelle Spectrograph (FOCES) (Pfeiffer et al. 1998) with a 2048 × 2048 24μ SITE#1d CCD detector on the 2.2 m telescope at the German Spanish Astronomical Observatory (CAHA) (Almería, Spain) to obtain spectra between 22 to 26 April 2002 and from 29 March to 7 April 2004. The wavelength range covers from 3450 to 10 700 Å in 112 orders. The reciprocal dispersion ranges from 0.04 to 0.13 Å/pixel and the spectral resolution (*FWHM*) ranges from 0.08 to 0.35 Å.

5) 2.56 m-NOT-SOFIN, Roque de los Muchachos Obs., 2004/04.
We used the 2.56 m Nordic Optical Telescope (NOT) located at the Observatorio del Roque de los Muchachos (La Palma, Spain) on 2 to 6 April 2004. We used The Soviet Finnish High Resolution Echelle Spectrograph (SOFIN) with an echelle grating (79 grooves/mm), ASTROMED-3200 camera and a 2052 × 2052 pixel 2K3EB PISKUNOV1 CCD detector. The wavelength range covered from 3545 to 10 120 Å in 42 orders. The reciprocal dispersion ranges from 0.033 to 0.11 Å/pixel and the spectral resolution (*FWHM*) from 0.14 to 0.32 Å. We note that we had some problems with the wavelength calibration, during the arc lamp spectra exposures, and as a consequence, could not rely on the absolute wavelength calibration of the spectra taken in this observing run. Therefore, these spectra have not been used to determine radial velocities, although we have used them for the remaining analysis.

In Table 1 we present the observing log. For each observation we list date, UT, and the signal to noise ratio (S/N) obtained in the Hα line region.

We extracted spectra using the standard reduction procedures in the IRAF[1] package (bias subtraction, flat-field division and optimal extraction of the spectra). The wavelength calibration was obtained by taking spectra of a Th-Ar lamp. Finally,

---

[1] IRAF is distributed by the National Optical Observatory, which is operated by the Association of Universities for Research in Astronomy, Inc., under contract with the National Science Foundation.

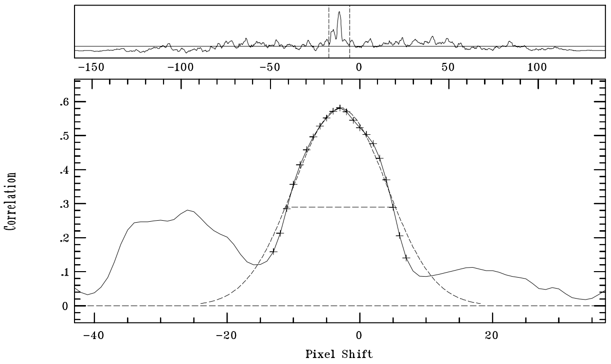

Fig. 1. CCF of FF UMa (2RE J0933+624) in FOCES04 observing run. Irregular profiles can be seen in the two peaks. These irregularities can produce significative errors in radial velocity determination.

we normalized the spectra by a polynomial fit to the observed continuum.

3. Orbital period variation

3.1. Radial velocities

We determined the heliocentric radial velocities by making use of cross-correlation technique (see Paper IV). The spectra of the target were cross-correlated order by order, using the routine FXCOR in IRAF, against spectra of radial velocity standards with similar spectral type taken from Beavers et al. (1979). We derived the radial velocity for each order from the position of peak of the cross-correlation function (CCF) and calculated the uncertainties based on the fitted peak height and the antisymmetric noise as described by Tonry & Davis (1979). As FF UMa is an SB2 system we note two peaks in the CCF, associated with the two components, and fit each one separately. When the components are too close, we used deblending fits. It is worth mentioning that the uncertainties returned by FXCOR for SB2 binaries are overestimated; when fitting each star, the presence of the other will increase the antisymmetric noise, thereby biasing the error.

As Fig. 1 shows, the irregular profiles of the CCF (double peaks and asymmetries) can produce significant errors in radial velocity measures. These irregularities may come from photospheric activity features on the stellar surface of both components that disturb the profile of the photospheric lines and induce variations in the peak of the CCF. However, this behavior may also be due to the difference in rotational velocity ($v \sin i$) between the problem and radial velocity star. When the spectrum of the standard star was broadened to the same rotational velocity of FF UMa ($v \sin i \approx 30$ km s^{-1}) the profiles of CCF become smoother and could be fit with a Gaussian profile, see Fig. 2. Therefore all the radial velocities given in this paper have been calculated by cross-correlation with this rotational broadened spectrum of the standard star.

In Table 2 we list, for each spectrum, the heliocentric radial velocities ($V_{\rm hel}$) and their associated errors (σ_V) obtained as weighted means of the individual values deduced for each order in the spectra. Those orders which contain chromospheric features and prominent telluric lines have been excluded when determining the mean velocity.

3.2. $T_{\rm conj}$ variations

With 35 radial velocity data from our measures and nine from Jeffries et al. (1995) (see Table 2), we computed the orbital solution of this system. Although we obtained good results when we fit orbital solution for each observing run data separately, some orbital parameters changed from one epoch to another. When we tried to fit the orbital solution with all the data, we could not find any satisfactory result.

Table 2. Radial velocities.

Obs.	HJD 2 400 000+	S/N (Hα)	Primary $V_{\rm hel} \pm \sigma_V$ (km s^{-1})	Secondary $V_{\rm hel} \pm \sigma_V$ (km s^{-1})
Jef(95)[1]	49054.591	-	23.5 ± 4.0	−35.9 ± 9.0
Jef(95)[1]	49054.634	-	26.8 ± 3.0	−30.0 ± 9.0
Jef(95)[1]	49054.675	-	22.6 ± 3.0	−45.0 ± 5.0
Jef(95)[1]	49055.378	-	20.0 ± 3.0	−53.3 ± 3.0
Jef(95)[1]	49055.423	-	19.5 ± 3.0	−47.6 ± 4.0
Jef(95)[1]	49056.425	-	−25.1 ± 5.0	48.7 ± 3.0
Jef(95)[1]	49056.486	-	−20.6 ± 4.0	58.8 ± 3.0
Jef(95)[1]	49056.543	-	−28.1 ± 4.0	57.8 ± 3.0
Jef(95)[1]	49056.600	-	−29.4 ± 4.0	57.3 ± 3.0
MCD98	50826.935	146	25.80 ± 1.92	−62.05 ± 4.75
MCD98	50827.915	203	−11.09 ± 6.26	26.23 ± 6.62
MCD98	50828.922	98	−22.16 ± 1.71	49.39 ± 4.58
MCD98	50829.929	139	25.95 ± 1.86	−60.06 ± 4.29
MCD98	50830.932	95	−1.88 ± 6.25	-
MCD98	50831.961	134	−28.27 ± 1.72	54.33 ± 4.59
MCD98	50832.958	146	17.88 ± 1.63	−50.03 ± 6.42
MCD98	50833.935	83	9.34 ± 4.51	−33.52 ± 4.72
MCD98	50834.953	77	−29.42 ± 1.78	55.83 ± 4.90
MCD98	50836.039	115	−4.99 ± 6.20	-
HET00	51561.943	-	−27.96 ± 2.60	61.98 ± 2.80
HET00	51562.759	233	−3.74 ± 6.51	-
HET00	51562.837	-	−2.75 ± 6.50	-
HET00	51566.774	263	24.78 ± 2.66	−62.86 ± 2.81
HET00	51566.797	-	25.66 ± 2.66	−65.02 ± 2.81
HET00	51567.812	83	−0.97 ± 6.21	-
HET00	51568.767	146	−31.61 ± 2.29	58.01 ± 2.70
HET00	51569.925	236	21.76 ± 2.64	−58.45 ± 2.53
FOCES02	52387.329	118	−31.89 ± 2.33	54.19 ± 4.49
FOCES02	52388.320	200	−2.24 ± 4.13	-
FOCES02	52389.323	140	24.44 ± 2.56	−54.03 ± 4.62
FOCES02	52390.414	146	−24.46 ± 2.63	47.34 ± 4.93
FOCES04	53096.4836	71	26.98 ± 2.58	−63.76 ± 6.27
FOCES04	53098.3186	63	−32.32 ± 2.06	58.08 ± 6.46
FOCES04	53099.3077	87	10.94 ± 3.24	−41.79 ± 8.17
FOCES04	53099.4736	74	19.50 ± 2.98	−51.18 ± 5.88
FOCES04	53099.6158	59	23.20 ± 2.31	−58.85 ± 6.54
FOCES04	53100.3048	95	18.38 ± 4.44	−41.31 ± 8.71
FOCES04	53100.4329	117	10.31 ± 4.15	−30.65 ± 8.26
FOCES04	53100.5718	80	0.24 ± 4.41	-
FOCES04	53101.3082	56	−31.11 ± 2.03	55.25 ± 5.04
FOCES04	53101.4374	122	−31.81 ± 2.44	58.15 ± 5.54
FOCES04	53101.5932	130	−32.02 ± 2.18	58.24 ± 5.44
FOCES04	53102.3061	117	−3.95 ± 4.25	-
FOCES04	53102.5640	93	11.02 ± 3.46	−40.39 ± 8.89

[1] JEF(95): Jeffries et al. (1995).

We decided to recalculate the orbital solution of each observing run, using the period obtained from the FOCES04 observing run and assuming a circular orbit (since e is only $\approx 10^{-2}$). We determined that the solutions are very similar except at time of conjunction, $T_{\rm conj}$, (see Fig. 3). Therefore we shifted in phase the solutions of every run taking as standard the FOCES04 solution. As we can see in Fig. 4, all data points are now in agreement with the orbital solution. We obtained the phase shift calculating the conjunction time differences between the conjunction time

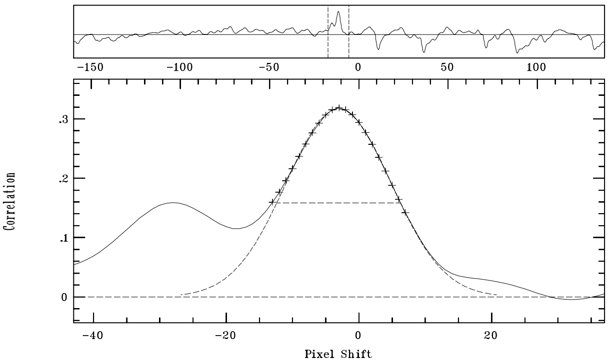

Fig. 2. CCF of FF UMa (2RE J0933+624) in FOCES04 observing run obtained when we broad the standard star to FF UMa rotational velocity. Irregular profiles become smoother and can be fitted with a Gaussian.

Table 3. Variations of orbital period (P).

Year	Tconj HJD (2400000 +)	O–C day	dP/P
1993	49055.8789	−2.0089	4.979×10^{-4}
1998	50824.4023	−1.1755	5.187×10^{-4}
2000	51561.2227	−0.9005	5.887×10^{-4}
2002	52386.6758	−0.3615	5.134×10^{-4}
2004	53090.8398		

obtained in every run fit and the conjunction time of FOCES04 run fit, (O–C) (Observed – Calculated = T_{conj} difference coming from orbital solution fit in each run and the FOCES04 run).

In Fig. 5, we represent the temporal variation of the O–C (T_{conj}) for every run. The maximum amplitude of the variation found in our data is 2 days and shows a decreasing linear tendency. We would need a longer temporal range of observations to test if the tendency remains linear or becomes sinusoidal as one might expect if there is a cycled behavior related with the activity cycle (see Frasca & Lanza 2005 and Sect. 3.3).

When the O–C (T_{conj}) variations are transformed to relative orbital period variations, we find d$P/P \approx 10^{-4}$ in 11 years, that is, one order of magnitude higher than the largest value observed until now in HR 1099 (see Table 3).

3.3. Discussion

To explain the behavior described above, we considered several options:

- First, we explore how the existence of a third distant star as a component of the system could modify the main orbit. In Fig. 6, we plotted the center of mass radial velocity, γ, obtained for each observing run, versus time.

  The amplitude of variations in γ amounted to 3 km s^{-1}, over 11 years. Such differences are large enough that they are unlikely to be due to zero-point (instrumental) differences between different runs. The variations in γ could indicate the presence of a third component; if the third star is small and its period long, the reflex motion of the binary will necessarily be small. As an example, using Eq. (30) from Cumming (2004), a third star with a mass between 0.4 and 0.6 $M_{\odot}$ and an orbital period of 20 to 40 yr in an edge-on circular orbit would produce a semi-amplitude K on the binary between 2.1 and 3.8 km s^{-1}. In addition, if the orbit were significantly eccentric, as is often the case for such long periods, the K amplitude could be larger. The presence of the third component could easily induce a change in γ similar to that observed. Therefore with the present data we cannot dismiss the possibility that these variations are due to a third body.
- Another explanation of our observations could be an orbital modulation due to the variation of activity with time, explained as a consequence of cyclical variations of the quadrupole-moment of both components of the system during the magnetic activity cycle. This mechanism presented by Matese & Whirtmere (1983) and developed by Applegate (1992) and Lanza et al. (1998), has been used in the study of several RS CVn systems such as SZ Psc (Kalimeris et al. 1995), RT Lac, RS CVn, WW Dra, etc. (Lanza & Rodonó 1999), XY UMa (Sowell et al. 2001) and HR 1099 (García-Álvarez et al. 2003; Frasca & Lanza 2005; Lanza 2006).

  Applegate (1992), described the initial model in which the orbital period variation is due to the gravitational coupling of the orbit to changes in the quadrupole moment (rotational oblateness) of a magnetically active star in the system. The quadrupole moment of a star is determined by the rotation rate of its outer layers – if angular momentum is transferred to the outer layers, they rotate faster and the star becomes more oblate. The gravitational acceleration varies if the shape varies; this shape variation is measured by the change of the quadrupole moment of the star. On the contrary, if the outer layers loses angular momentum, the oblateness decreases. As the dynamo mechanism implies the qualitative shearing of magnetic field by differential rotation, the last should vary through the activity cycle. Applegate (1992) says that quantitatively, a subsurface magnetic field of several kilogauss can exert a large enough torque to transfer the angular momentum needed to make the observed period changes.

  Lanza et al. (1998) studied several possibilities of the process to explain the period variations in RS CVn systems with different kind of dynamos. They showed that variations of about 100 Gauss in a poloidal magnetic field could produce the observed variations, while Applegate suggested variations in order of kilogauss. Lanza & Rodonó (1999) compiled 46 binary systems of different types (RS CVn, WW UMa, etc.) to evaluate the effects of the quadrupole moments change.

  Lanza (2005), analyzes the Applegate model predictions and the observed results in RS CVn stars. He suggested that the model should be rejected because it fails to explain the orbital period variations of classical RS CVn close binary systems. The required variation of the internal differential rotation is too large to both agree with the observations and oppose turbulent dissipation. He concludes that any similar hypothesis to explain this phenomenon should include the effect of the Lorentz force on the gravitational quadrupole moment, or, that an entirely new theoretical framework is needed to interpret the observed orbital period variations in magnetically RS CVn binaries.

  Based on the Lanza (2005) review of the Applegate model, Frasca & Lanza (2005) and Lanza (2006), continued with the characterization of the orbital period variation of HR 1099. They suggested that there is an interaction between the magnetic fields of the K1 IV subgiant (primary component), and the magnetic fields of the G5 V component (secondary). In the primary, the hydromagnetic dynamo action is maintained in the deep fast-rotating convective envelope, while in the

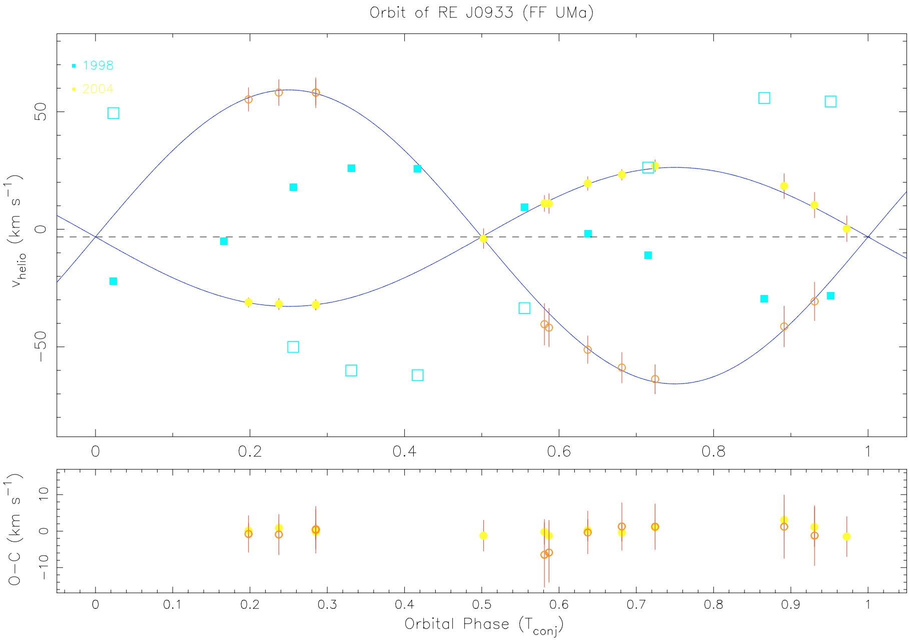

Fig. 3. Example of the phase shift between orbital solution of FOCES04 and McDonald98 observing runs. Radial velocities and orbital fit (solid line) of FOCES04 is plotted and radial velocities of McDonald98 are superimposed. Filled symbols correspond to primary and open symbols to secondary.

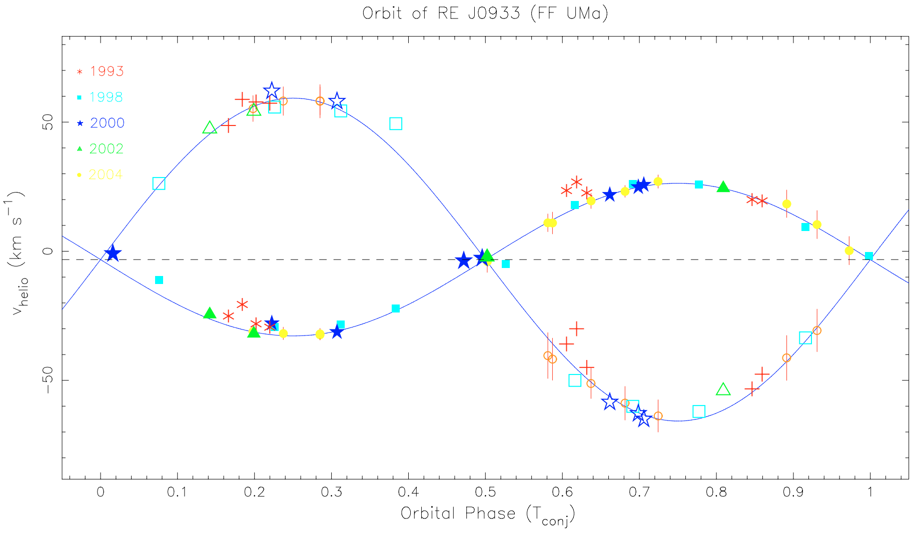

Fig. 4. Radial velocities of all observing runs. The orbital solution fit of FOCES04 observing run is plotted here (solid line) and the radial velocities of the rest runs (shifted in phase) are superimposed. See text for explanation (Sect. 3.2).

secondary, the magnetic field comes from an outer convection zone with a smaller radial extension, implying that its dynamo is less efficient (reflected by its lower level of activity). They argued that the Applegate classic model could not explain the variation found while their assumptions of the relation between orbital period cycle and the activity cycle could explain the large variation measures. They mention, however, the need to verify their claim with a larger study including other systems.
Summing up, the results found until now indicate that variations in the orbital period based on the Applegate model should be revised and that the strong temporal activity observable changes could reflect the relation between the orbital period variations and the changes in magnetic field and gravitational quadrupolar moment. The variations found in previous RS CVn systems are about $\mathrm{d}P/P \approx 10^{-6}$–$10^{-5}$ in a 7 to 109 years range.
The high level of chromospheric activity of both components of FF UMa (spectral types K1 IV and K0 V, see Sects. 4.2 and 5) could imply a strong interaction between larger and more efficient dynamos. This could explain the order of magnitude difference between the orbital period variation of this system and the one detected in other RS CVn systems like HR 1099.

- Finally, although the above explained activity-related period variation is our preferred interpretation, we should mention that in the case of the presence of a third component, there could well be changes in the elements of the inner orbit. If the eccentricity were small but non-zero there could be apsidal motion in the binary due to the third body and the change in the longitude of periastron would be seen as a change in the time of conjunction.

3.4. Orbital solution

As a consequence of the results in Sects. 3.2 and 3.3, we have computed the orbital solution of this system using radial velocity data from the FOCES04 observing run. We chose this run because it has a large number of data points (13) and superior spectral resolution. The radial velocity data are plotted in Fig. 4. Solid symbols represent the primary and open symbols represent the secondary. Each observing run is represented with a different

Table 4. Orbital solution.

Element	Value	Uncertainty	Units
$P_{\rm orb}$	3.274	0.054	days
$T_{\rm conj}$	53 090.84	0.18	HJD (2 400 000+)
ω	0.00	0.00	degrees
e	0.00	0.00	(adopted)
$K_{\rm P}$	29.55	0.95	km s^{-1}
$K_{\rm S}$	62.52	3.60	km s^{-1}
γ	−3.23	0.77	km s^{-1}
$q = M_{\rm P}/M_{\rm S}$	2.12	0.10	
$a_{\rm P} \sin i$	1.330	0.048	10^6 km
$a_{\rm S} \sin i$	2.81	0.17	10^6 km
$a \sin i$	4.14	0.18	10^6 km
"	0.028		AU
"	5.95		$R_\odot$
$M_{\rm P} \sin^3 i$	0.180	0.024	$M_\odot$
$M_{\rm S} \sin^3 i$	0.085	0.012	$M_\odot$
$f(M)$	0.00875	0.00099	$M_\odot$

symbol. The curve represent a minimum χ^2 fit orbit solution. The orbit fitting code uses the *Numerical Recipes* (Press et al. 1986) implementation of the Levenberg-Marquardt method of fitting a non-linear function to the data, which weights each datum according to its associated uncertainty. The program simultaneously solves for the orbital period, $P_{\rm orb}$, the epoch of periastron passage, $T_{\rm conj}$, the longitude of periastron, ω, the eccentricity, e, the primary star's radial velocity amplitude, $K_{\rm P}$, the heliocentric center of mass velocity, γ, and the mass ratio, q. The orbital solution and relevant derived quantities are given in Table 4. In this table, we give $T_{\rm conj}$ as the heliocentric Julian date of conjunction with the hotter star behind the cooler star, in order to adopt the same criteria used in previous papers. We used this criterion to calculate the orbital phases of all the observations reported in this paper.

This binary results in a circular orbit (adopted) with an orbital period of about 3.274 days. Since $P_{\rm phot} \approx 3.270$ days, we can say that it is a synchronous system. The mass ratio of 2.12 calculated let us conclude that the components have a different spectral type. The obtained parameters are in agreement with the values reported by Jeffries et al. (1995).

4. Stellar parameters of the binary system

We give the adopted stellar parameters of FF UMa in Table 5. The photometric data ($B-V$, V, $P_{\rm phot}$) are taken from SIMBAD, Jeffries et al. (1995), Henry et al. (1995) and Strassmeier et al. (2000). Orbital period ($P_{\rm orb}$) and projected rotational velocity ($v \sin i$) have been determined in this paper (see Sects. 3.4 and 4.1). The astrometric data (parallax, π; proper motions, $\mu_\alpha \cos\delta$ and μ_δ) are from Hipparcos (ESA 1997) and Tycho-2 (Høg et al. 2000) catalogues.

4.1. Spectral types and other derived parameters

To obtain the spectral type of this binary system we compared our high resolution echelle spectra, in several spectral orders free of lines sensitive to chromospheric activity, with spectra of inactive reference stars of different spectral types and luminosity classes observed during the same observing run. This analysis makes use of the program STARMOD developed at Penn State University (Barden 1985) which we modified later. This program constructs a synthesized stellar spectrum from artificially rotationally broadened, radial-velocity shifted, and weighted spectra of appropriate reference stars.

For FF UMa we obtained the best fit between observed and synthetic spectra using a K1IV reference star for primary component and a K0V for the secondary, with a contribution to the continuum of 0.70 and 0.30 respectively. These spectral types are in agreement with the results reported by other authors who suggested an evolved component. In our spectra, the spectral features indicate strongly the subgiant nature of the primary.

We note that since the primary component is a subgiant star, the stellar parameters, such us mass and radius, cover a wide range of values. Therefore, we determined these crucial characteristics using data from the secondary star. Assuming a K0V spectral type for secondary component, we adopted from Landolt-Börnstein tables (Schmidt-Kaler 1982) a mass $M_{\rm S} = 0.79\ M_\odot$ and, according to the mass ratio from the orbital solution ($q = 2.12$), we derived a primary mass of $M_{\rm P} = 1.67\ M_\odot$.

In addition, from the photometric period (3.27 days) given by Henry et al. (1995) and the rotational velocity, calculated here, $v \sin i_{\rm P} = 33.57$ km s^{-1} (Sect. 4.2), we estimated a minimum radius of $R \sin i_{\rm P} = 2.17\ R_\odot$. This agrees with the subgiant radii and previous estimations.

4.2. Rotational velocities

Jeffries et al. (1995) estimated the projected rotational velocity ($v \sin i$) as 41 km s^{-1} for the primary component and as 32 km s^{-1} for the secondary. Fekel (1997) obtained 38.8 and 39.7 km s^{-1} for each component and Strassmeier et al. (2000) reported lower values, 17 and 16 km s^{-1} respectively.

By using the program STARMOD we obtained the best fits for each observing run using $v \sin i$ values os $\approx$35 km s^{-1} for primary component and $\approx$38 km s^{-1} for secondary component.

To determine a more accurate rotational velocity of this star we made use of the cross-correlation technique in our high resolution echelle spectra by using the routine FXCOR in IRAF. The method is described carefully in previous papers (see Gálvez et al. 2002; López-Santiago et al. 2003) and is based on the fact that when a stellar spectrum with rotationally broadened lines is cross-correlated against a narrow-lined spectrum, the width of the cross-correlation function (CCF) is sensitive to the amount of rotational broadening of the first spectrum.

As a template star in this process we used the K1V star HD 26965 for the primary component and the K0V star HD 3651 for the secondary for the McDonald run and the K2V star HD 166620 for both components in the remaining runs. All these stars have very low rotation velocity -less than 3 km s^{-1}. The averaged values obtained are $v \sin i = 33.57 \pm 0.45$ and 32.38 ± 0.75 km s^{-1} for primary and secondary components respectively.

4.3. Kinematics

Computing the galactic space-velocity components (U, V, W) of FF UMa required both radial velocity and precise proper motions and parallax. For the former, we used the center of mass velocity, γ, determined in the orbital solution for the FOCES04 observing run (see Sect. 3.4). For the latter we utilized data taken from Hipparcos (ESA 1997) and Tycho-2 (Høg et al. 2000) catalogues (see Table 5, for details see Montes et al. 2001a,b).

Table 5. Stellar parameters of FF UMa.

$T_{\rm sp}$	SB	$B-V$	$V-R$	$P^1_{\rm orb}$ (days)	$P_{\rm phot}$ (days)	$v \sin i^1$ (km s^{-1})	π (mas)	$\mu_\alpha \cos \delta$ (mas/yr)	μ_δ (mas/yr)
K0V/K0IV[1]	2	0.97	0.75	3.274[1]	3.27	33.57[1] ± 0.45/32.38[1] ± 0.75	9.57 ± 0.92	−21.20 ± 1.30	−23.00 ± 1.60

[1] Values determined in this paper.

Table 6. Galactic space-velocity components.

$U \pm \sigma_U$ (km s^{-1})	$V \pm \sigma_V$ (km s^{-1})	$W \pm \sigma_W$ (km s^{-1})	$V_{\rm Total}$ (km s^{-1})
−7.04 ± 1.14	−12.92 ± 1.33	−6.68 ± 0.68	16.16

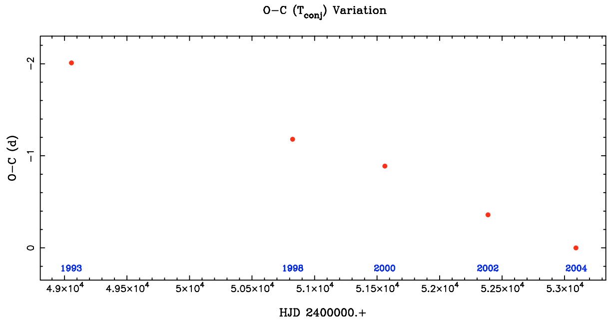

Fig. 5. The (O–C) (Observed−Calculated $T_{\rm conj}$) versus Heliocentric Julian date HJD for every observing run.

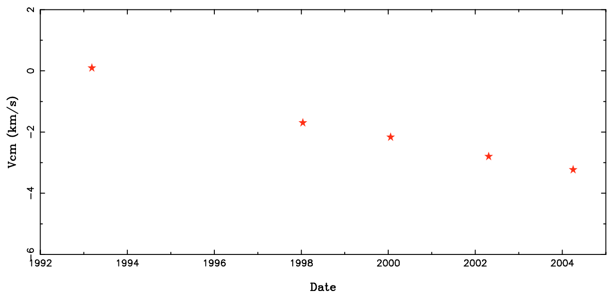

Fig. 6. Center of mass velocity, γ, obtained in each observing run fit versus time.

In addition, we included FF UMa in an extended study of binary star kinematics in young moving groups. It included the application of Eggen's peculiar velocity and radial velocity criteria (see Montes et al. 2001a, and reference therein) and spectroscopic criteria (see the Li I λ6707.8 line Sect. 4.4).

The resulting values of (U, V, W) and associated errors are given in Table 6. These errors have been calculated assuming the value of γ determined from the FOCES04 observing run. However, taking into account the changes in $\gamma \approx 3$ km s^{-1} we detected, we expect the uncertainties to be larger (see Sect. 3.3).

Using the (U, V) and (V, W) diagrams (Eggen 1984, 1989; Montes et al. 2001a), the velocity components lie clearly inside the Castor moving group boundaries. In addition, Eggen's radial velocity criteria also confirm their membership of FF UMa to this group (Gálvez 2005).

4.4. The Li I λ6707.8 line

As it is well known, Li I λ6707.8 spectroscopic feature is an important diagnostic of age in late-type stars, since it is destroyed easily by thermonuclear reactions in the stellar interior.

The spectral region of the resonance doublet of Li I at λ6708 Å is covered by most of our spectral observations. Despite blending with photospheric lines, mainly Fe I (6707.4 Å), we could separate the contribution from both components. We then measured the equivalent width (EW hereafter) of (Li I + Fe I) of both components in our observed spectra. We calculated the contribution of Fe I by using both calibrations of Fe I-effective temperature from Soderblom et al. (1990) and Fe I-($B-V$) color index from Favata et al. (1993). We obtained the corrected EW(Li I) by subtracting the EW(Fe I) of the total measured equivalent width, EW(Li I+Fe I). The resulting mean values of EW(Li I) are 200 mÅ for the primary component and 141 mÅ for the secondary. These values are corrected by the contribution of each component to the continuum (see Sect. 5).

By using the spectral subtraction technique, that is, obtaining the EW of Li I directly from the subtracted spectra, we obtained a mean EW(Li I) of 132 mÅ and 86 mÅ for both component respectively.

The discrepancy between the two methods used to calculate the EW is due to the influence of stellar metallicities. In the first technique, stellar metallicity is not taken into account in the relation calibrations, and in the second technique, the stellar metallicity of the standard star used to create the synthetic spectra is undetermined. In spite of this, these EW(Li I)s values are of the same order as the Li I EWs of other Castor moving group members, which have an age around 200 Myr.

5. Chromospheric activity indicators

The echelle spectra analyzed allow us to study the behavior of the Ca II H & K to the Ca II IRT lines, different indicators formed at varying atmospheric heights. We determined the chromospheric contribution of these features using the spectral subtraction technique described in detail by Montes et al. (1995) and Papers I–IV. We constructed the synthesized spectrum using the program STARMOD.

Taking into account the stellar parameters derived in Sect. 4 we used reference stars of the K1IV spectral type for the primary component and K0V spectral type for the secondary component (see Sect. 4.3), with a contribution of 0.70/0.30 respectively.

In Table 7 (only available in electronic form) we present the excess emission EW, measured in the subtracted spectra, for the Ca II H & K, Hϵ, Hδ, Hγ, Hβ, Hα, and Ca II IRT lines in all observing runs. We list the EWs of emission features for both components (P/S); when lines were blended we list only total EWs. The uncertainties in the measured EW were estimated taking into account:

a) the typical internal precisions of STARMOD (0.5–2 km s^{-1} in velocity shifts, and ±5 km s^{-1} in $v \sin i$);

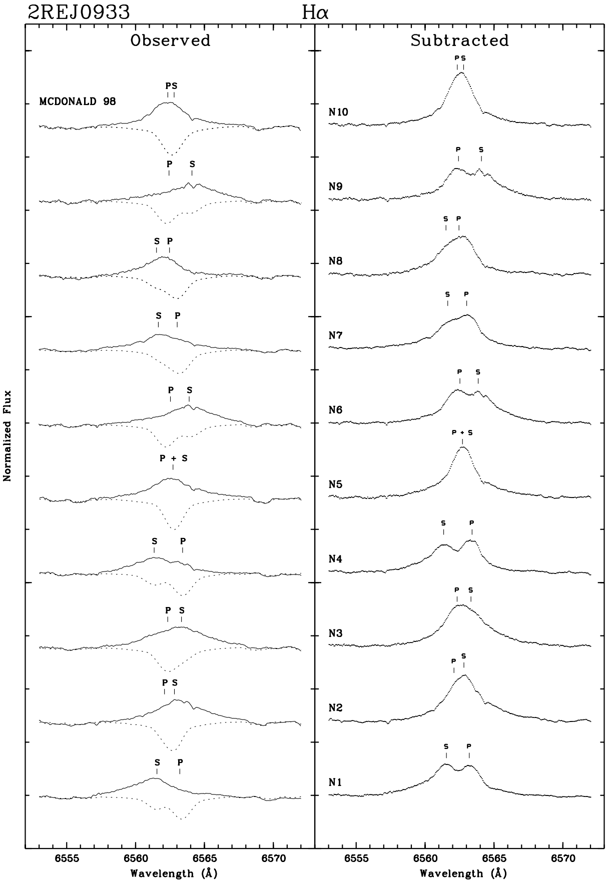

Fig. 7. Spectra in the Hα line region in McDonald98 observing run. We plot the observed spectrum (solid-line) and the synthesized spectrum (dashed-line) *in the left panel*, and the subtracted spectrum (dotted line), *in the right panel*. We mark position of primary component lines with a (P) and position of secondary component lines with a (S).

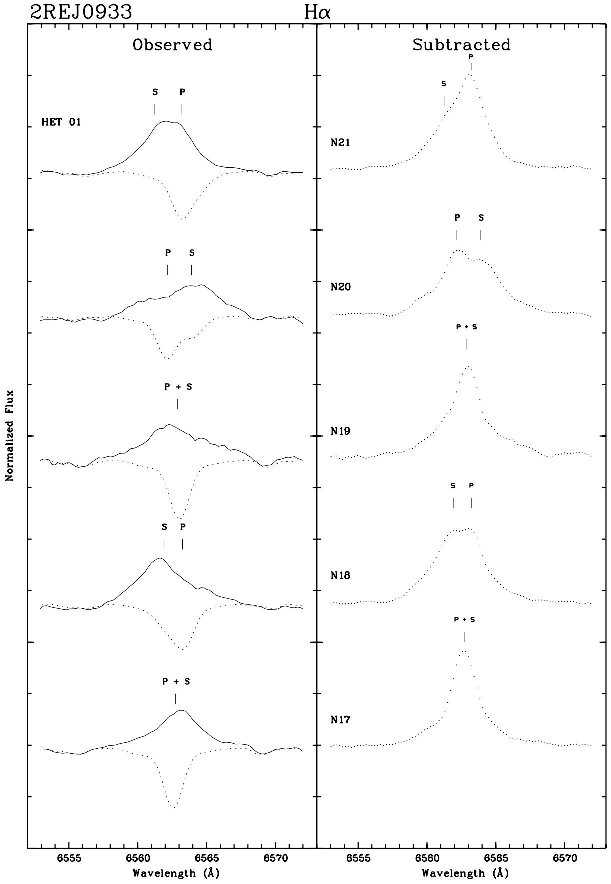

Fig. 8. The same as in previous figure in HET00 observing run.

b) the rms obtained in the fit between observed and synthesized spectra in the spectral regions outside the chromospheric features (typically in the range 0.01–0.03); and
c) the standard deviations of the EW measurements.

The final estimated errors are in the range 10–20%.

We corrected the measured EWs for the relative contribution of each component to the total continuum (S_P and S_S), using the radii assumed in Sect. 4.1. and temperatures from Landolt-Börnstein tables (Schmidt-Kaler 1982). We obtained the final EWs for the components multiplying by a factor $1/S_P$ and $1/S_S$, respectively. We present the result in Table 7.

These adopted EWs were transformed to absolute surface fluxes using the empirical stellar flux scales calibrated by Hall (1996) as a function of the star color index. We used the $B-V$ index and the corresponding coefficients for Ca II H & K, Hα and Ca II IRT. We used for Hϵ the same coefficients as for Ca II H & K, and derived the Hδ, Hγ and Hβ coefficients of flux by making an interpolation between the values of Ca II H & K and Hα. We present the logarithm of the obtained absolute flux at the stellar surface ($\log F_S$) for the different chromospheric activity indicators in Table 8 (only available in electronic form). In Figs. 7–15 we plot the Hα, Ca II H & K and Ca II IRT λ8498, λ8542 lines region for each observation, the observed spectrum (solid-line) and the synthesized spectrum (dashed-line) in the left panel and the subtracted spectrum (dotted line) in the right panel. We included the observing run of each spectrum in these figures. In Fig. 18, we plot a representative subtracted spectrum of FF UMa in the Hβ line region.

5.1. Hα

The Hα line is observed in emission above the continuum in all the spectra (see Figs. 7–11, left panel). In the observed spectrum, the emission associated with the secondary is larger than that associated with the primary. However, after applying the spectral subtraction technique, the Hα emissions above the continuum coming from both components are similar and in some cases the primary one is larger. The Hα emission is persistent during all observations indicating that it is a very active binary system similar to RS CVn and BY Dra systems that always show Hα emission above the continuum. Measuring the EW of this line, we found that each stellar component is formed by a central narrow component and a broad component that moves from red to blue. These are an indication of microflare activity (see Papers I–III). While we were able to separate the narrow components, we were unable to deblend the broad ones. Therefore, to determine the contribution of each stellar component to the total excess emission, we fit the narrow and broad component of each star together (see Figs. 16 and 17).

The EW average value measured in the subtracted spectra is $EW(\mathrm{H}\alpha) = 1.64/2.47$ Å for the primary and secondary components. We note that these are higher values than those reported by Jeffries et al. (1995). In Table 7 we list the EW of each stellar component determined by the fit described above. We also list the total EW (primary + secondary) determined by integrating the total excess emission profile. We note that Hα line shows

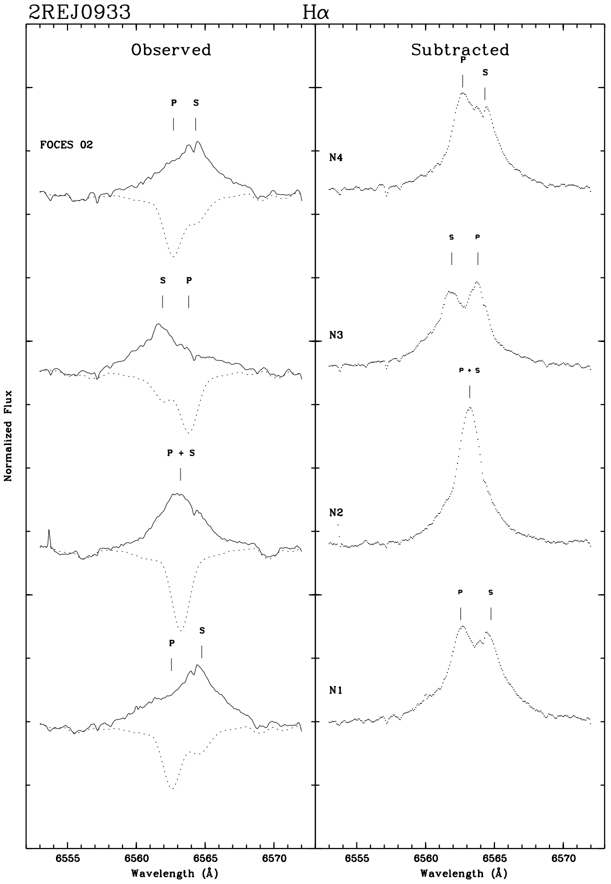

Fig. 9. The same as in previous figure in FOCES02 observing run.

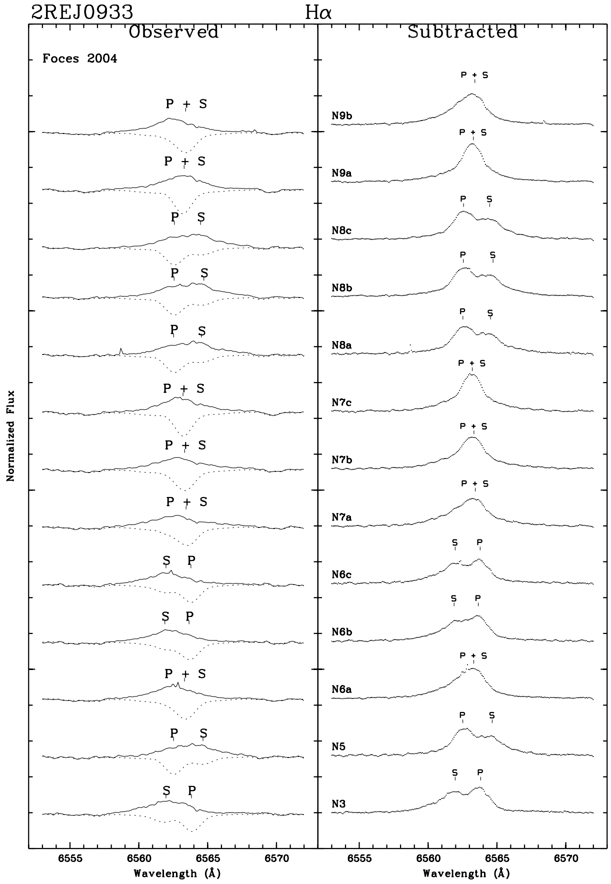

Fig. 10. The same as in previous figure in FOCES04 observing run.

notable variations with orbital phase but also from one epoch to another in both components.

5.2. Hβ, Hγ and Hδ

We can see absorption of Hβ, Hγ and Hδ Balmer lines filled in with emission in the observed spectra. After applying the spectral subtraction, clear excess emission is detected from both components (see a representative spectrum in the Hβ line region in Fig. 18). When the S/N was high enough we deblended the emission coming from both components by using a two-Gaussian fit to the subtracted spectra (see Table 7). These three lines show the same behavior with orbital phase that the Hα line in both components. Their mean values are $EW(\mathrm{H}\beta)$ = 0.33/0.25 Å, $EW(\mathrm{H}\gamma)$ = 0.14/0.19 Å and $EW(\mathrm{H}\delta)$ = 0.13/0.15 Å.

We also measured the ratio of excess emission in the Hα and Hβ lines, $\frac{EW(\mathrm{H}\alpha)}{EW(\mathrm{H}\beta)}$, and the ratio of excess emission $\frac{E_{\mathrm{H}\alpha}}{E_{\mathrm{H}\beta}}$ with the correction:

$$\frac{E_{\mathrm{H}\alpha}}{E_{\mathrm{H}\beta}} = \frac{EW(\mathrm{H}\alpha)}{EW(\mathrm{H}\beta)} * 0.2444 * 2.512^{(B-R)}$$

given by Hall & Ramsey (1992). This takes into account the absolute flux density in these lines and the color difference in the components. We obtained mean values of $\frac{E_{\mathrm{H}\alpha}}{E_{\mathrm{H}\beta}} \approx 6$ for the primary component and ≈5 for the secondary. These values indicate, according to Buzasi (1989) and Hall & Ramsey (1992), the presence of prominence-like material above the stellar surface in both components of the system.

5.3. Ca II H & K and Hε

The Ca II H & K line region is included in FOCES 2002 and 2004 and NOT04 observing runs.

This spectral region is located at the end of the echellogram, where the efficiency of the spectrograph and the CCD decrease very rapidly and therefore the S/N ratio obtained is very low; thus the normalization of the spectra is very difficult. In spite of this, the spectra show strong emission in the Ca II H & K lines and a clear emission in the Hε line from both components (see Fig. 12). These allow us to apply the spectral subtraction in this spectral region. As we can see in Fig. 12, the Hε line arising from one of the component overlaps with the Ca II H line arising from the other component at some orbital phases, so their EW were measured with a Gaussian fit when it was possible. Mean EWs values measured in these spectra are EW= 1.23/1.14 Å for each component in Ca II K line, EW= 1.23/1.08 Å in Ca II H line and EW= 0.30/0.43 Å in Hε line.

As the Hα emission line, the Ca II H & K lines show variations with both orbital phase and from one epoch to another in both components.

5.4. Ca II IRT lines (λ8498, λ8542 and λ8662)

All our echelle spectra include the three lines of the Ca II infrared triplet (IRT) except for the λ8498 line in HET00 and NOT04 runs. In all of the spectra we observed a clear emission above the continuum in the core of the Ca II IRT absorption lines (see Figs. 13–15) from both components. After applying the spectral subtraction, we could see that the emission coming

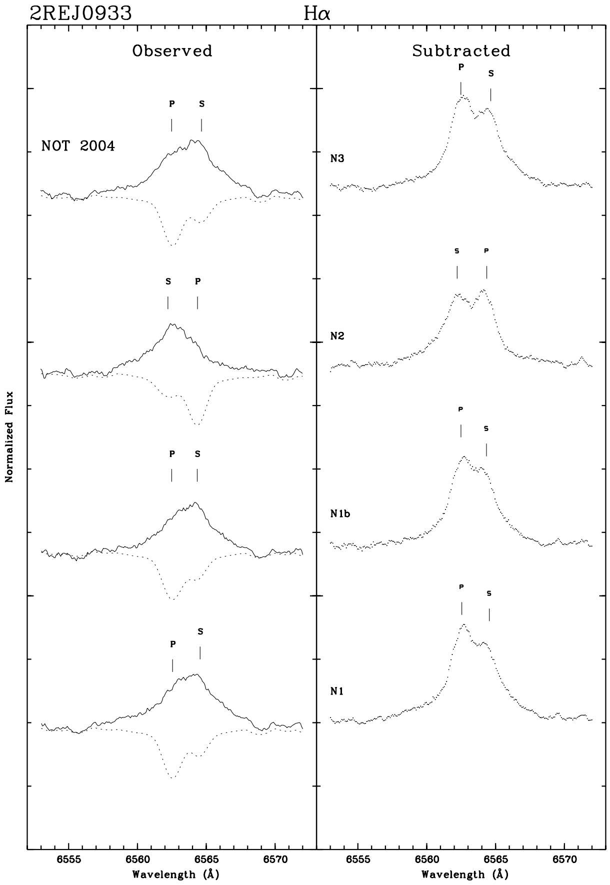

Fig. 11. The same as in previous figure in NOT04 observing run.

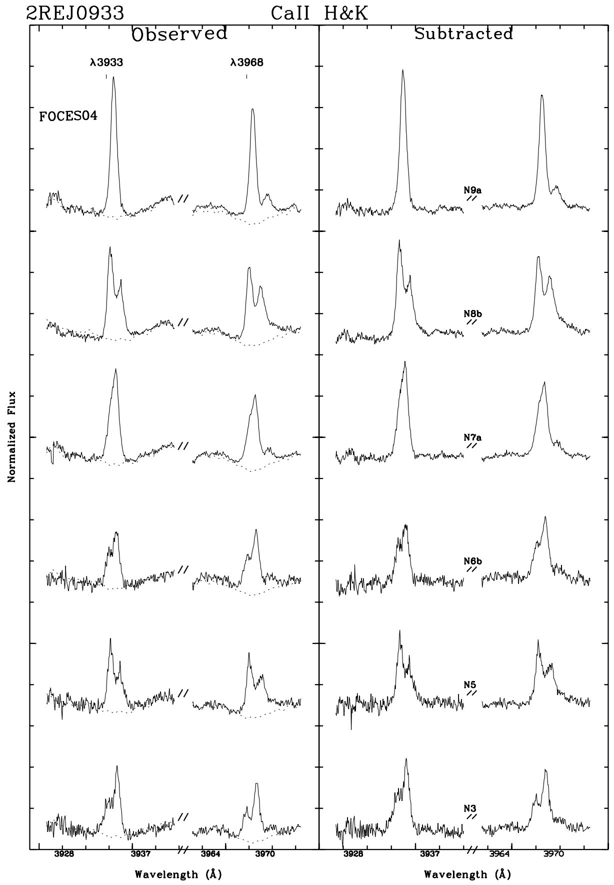

Fig. 12. The same as previous figure in Ca ii H & K line region in FOCES04 observing run.

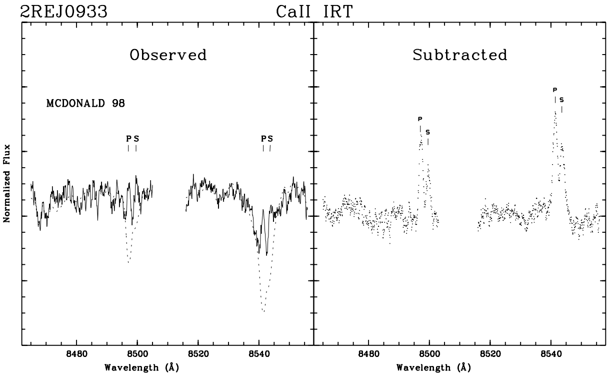

Fig. 13. The same as in previous figures but in Ca ii IRT (λ8498 and λ8542) line regions in McDonald98 observing run.

from the primary component is larger than the emission from the secondary.

We measured mean *EW*s for these three Ca ii lines of $EW(\lambda8498, \lambda8542, \lambda8662) = 0.58/0.35$, 0.67/0.43 and 0.59/0.35 Å respectively. For each component we found considerable variations with orbital phase that appear anti-correlated with the variations in the Balmer lines.

In addition, we calculated the ratio of excess emission *EW*, $\frac{E_{8542}}{E_{8498}}$, which is also an indicator of the type of chromospheric structure that produces the observed emission; in solar plages, values of $\frac{E_{8542}}{E_{8498}} \approx 1.5$–3 are measured, while in solar prominences the values are $\approx$9, the limit of an optically thin emitting plasma (Chester 1991). We found for this star small values of the $\frac{E_{8542}}{E_{8498}}$ ratio, $\approx$1.0, for both components (see Table 8). This indicates that the Ca ii IRT emission of this star arises from plage-like regions at the stellar surface, in contrast with the Balmer lines that come from prominences. This markedly different behavior of the Ca ii IRT emission has also been found in other chromospherically active binaries (see Papers III, IV and references therein).

5.5. Variation of activity with time

As we mentioned above, the *EW* emission lines that are chromospheric indicators show variations with orbital phase due to activity features present in both stellar surfaces. But there are also variations from one epoch to another in both components. To study if there is a correlation between active cycle and orbital period variation as Lanza (2006) suggested for the case of HR 1099, we must have a follow up of this system during a complete cycle of its variation period ($\geq$22 years). This kind of study would provide us another clue for understanding and testing the Applegate's mechanism.

6. Conclusions

In this paper, we present a detailed spectroscopic analysis of a X-ray/EUV selected chromospherically active binary system 2RE J0933+624 (FF UMa). We analyzed high resolution echelle spectra that include the optical chromospheric activity indicators from the Ca ii H & K to Ca ii IRT lines, as well as the Li i λ6707.8 line and other photospheric lines of interest.

With a large number of radial velocities from the literature and from our spectra taken over several years, we found that

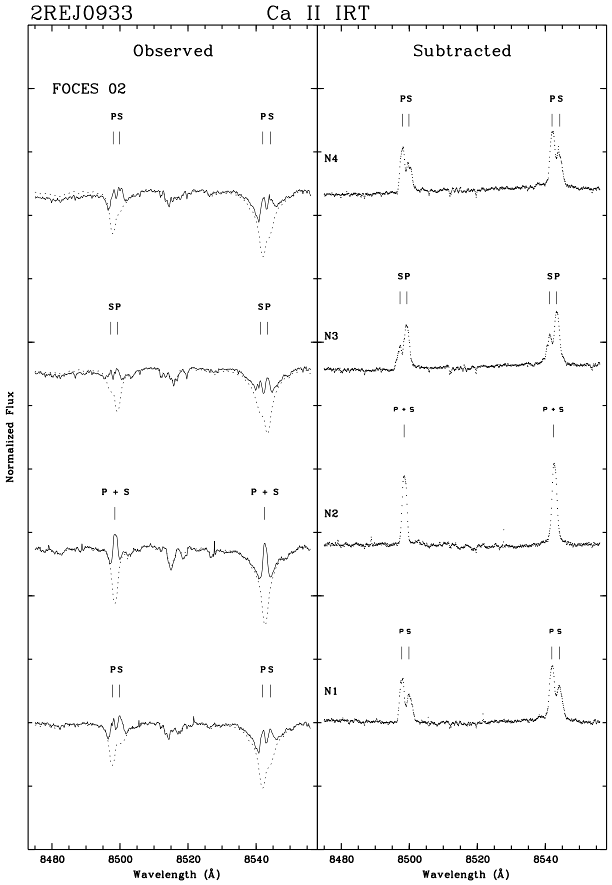

Fig. 14. The same as previous figure in FOCES02 observing run.

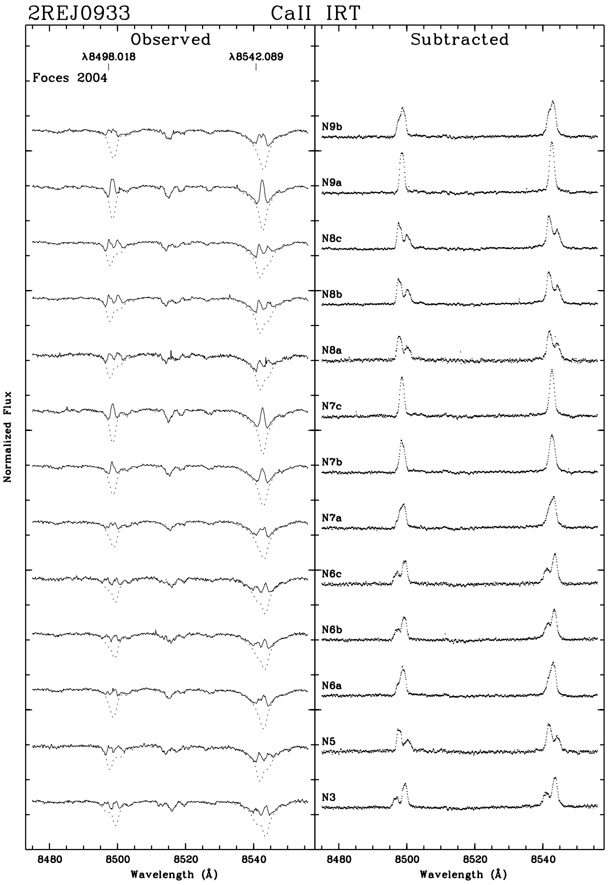

Fig. 15. The same as previous figure in FOCES04 observing run.

this system shows an orbital period variation similar to those previously found in other RS CVn systems.

Although the existence of an unseen distant third star as a component of the system cannot be completely ruled out as the cause of these variations, we think that the more plausible explanation is Applegate's mechanism, or at least the qualitative idea; which states that the orbital period change is due to the gravitational coupling of the orbit to changes in the quadrupole moment of the magnetically active stellar components of the system. In the case of FF UMa, we calculated a (O–C) ($T_{\rm conj}$) that gives us a relative orbital period variation of $\mathrm{d}P/P \approx 10^{-4}$ in 11 years, that is, one order of magnitude higher than the variations in HR 1099, the largest observed until now. We suggest here that this order of magnitude difference between the period variations in FF UMa and HR 1099 could be explained by the different activity level. The components of FF UMa are very active and have more effective dynamo mechanisms than HR 1099 components.

Once we adopted an orbital period, from the FOCES04 observing run, we improved the determination of the orbital solution of the system relative to previous determinations by other authors. We obtained a nearly circular orbit with an orbital period very close to photometric period, indicating that it has a synchronous rotation.

The spectral classifications derived by comparing FF UMa with spectra of reference stars, leads us to consider the primary component as a subgiant star and the secondary component as a K0V star. The results from orbital parameters and photometric characteristics help us to obtain physical parameters from the primary, $M_{\rm P} = 1.67\ M_{\odot}$ and $R \sin i_{\rm P} = 2.17\ R_{\odot}$, in agreement with subgiant radii and previous estimates.

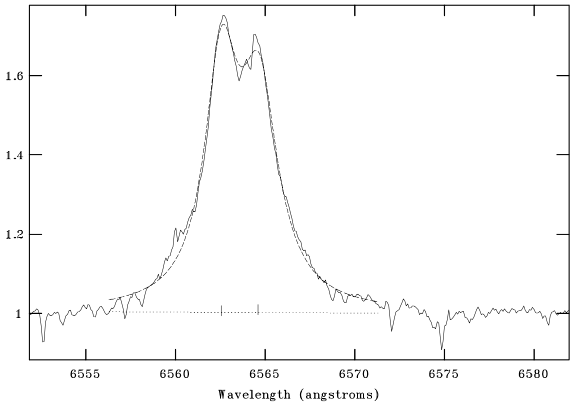

Fig. 16. Example of the Hα region fit in the subtracted spectrum of the two components by using IRAF *SPLOT* task.

By using the information provided by the width of the cross-correlation function we determined a projected rotational velocity, $v \sin i$, of 33.57 ± 0.45 km s^{-1} and 32.38 ± 0.75 km s^{-1} for the primary and secondary components respectively.

The presence of the Li I line is in agreement with the kinematics results, i.e., it belongs to the young disk and is probably a member of the Castor moving group.

The study of the optical chromospheric activity indicators shows that FF UMa system has a high level of activity in both components. The variation of Hα and the rest of the Balmer and Ca II H&K lines are very similar and anti-correlated in phase with Ca II IRT emission, as we confirmed with the $\frac{E_{\rm H\alpha}}{E_{\rm H\beta}}$ and $\frac{E_{8542}}{E_{8498}}$ results. This indicates that the Balmer emission lines

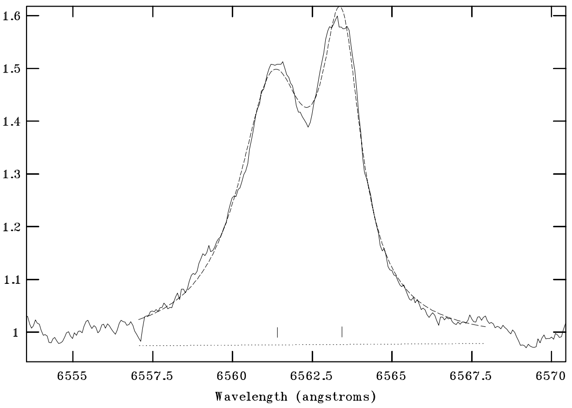

Fig. 17. Another example of Hα region fit.

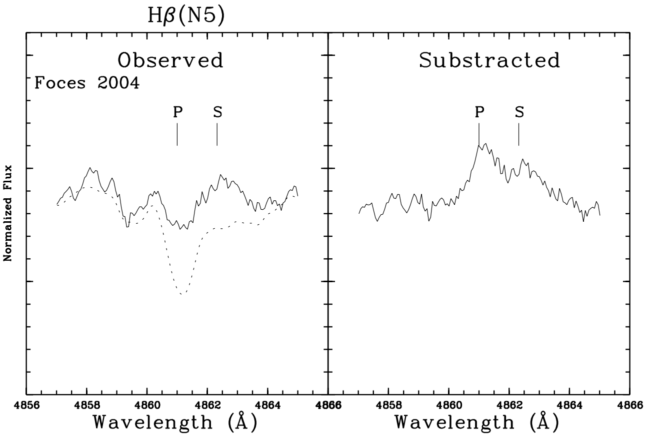

Fig. 18. The same as Hα figures but in Hβ line region in FOCES04 observing run.

arise from prominence-like material while the emission of Ca II IRT lines arise from plage-like regions. In addition, both components show variations from one epoch to another that could have a correlation with the orbital period variation. Future spectroscopic and photometric studies of this system could confirm this hypothesis and provide a better understanding and test of Applegate's mechanism.

Acknowledgements. We would like to thank Dr. L.W. Ramsey for collaborating on the McDonald observing runs (2.1 m and HET telescopes) and the staff of McDonald observatory for their allocation of observing time and their assistance with our observations. We thank Michelle L. Edwards for her help in checking and correcting the English writing. Finally, we want to thank the anonymous referee for very useful comments. This work was supported by the Universidad Complutense de Madrid and the Spanish Ministerio Educación y Ciencia (MEC), Programa Nacional de Astronomía y Astrofísica under grant AYA2005-02750 and the "Comunidad de Madrid" under PRICIT project S-0505/ESP-0237 (ASTROCAM).

References

Applegate, J. H. 1992, ApJ, 365, 621
Barden, S. C. 1985, ApJ, 295, 162
Beavers, W. I., Eitter, J. J., Ketelsen, D. A., & Oesper, D. A. 1979, PASP, 91, 698
Buzasi, D. L. 1989, Ph.D. Thesis, Pennsylvania State Univ.
Chester, M. M. 1991, Ph.D. Thesis, Pennsylvania State Univ.
Cumming, A. 2004, MNRAS, 354, 1165
Eggen, O. J. 1984, ApJS, 55, 597
Eggen, O. J. 1989, PASP, 101, 366
ESA 1997, The Hipparcos and Tycho Catalogues, ESA SP-1200
Favata, F., Barbera, M., Micela, G., & Sciortino, S. 1993, A&A, 277, 428
Fekel, F. C. 1997, PASP, 109, 514
Frasca, A., & Lanza, A. F. 2005, ApJ, 429, 309
Gálvez, M. C. 2005, Ph.D. Thesis, Universidad Complutense de Madrid
Gálvez, M. C., Montes, D., Fernández-Figueroa M. J., et al. 2002, A&A, 389, 524 (Paper IV)
García-Álvarez, D., Foing, B. H., Montes, D., et al. 2003, A&A, 397, 285
Gálvez, M. C., Montes, D., Fernández-Figueroa, M. J., De Castro, E., & Cornide, M. 2006, SEA/JENAM 2004, The many scales in the Universe, Joint European and National Astronomy Meeting, ed. J. C. Del Toro Iniesta, et al. Springer, Session 3, CD P29
Gálvez, M. C., Montes, D., Fernández-Figueroa, M. J., De Castro, E., & Cornide, M. 2007, Proceedings of Binary Stars as Critical Tools and Tests in Contemporary Astrophysics, IAU Symp. 240, 26th meeting of the IAU, Special Session 3, S240, 214
Hall, J. C. 1996, PASP, 108, 313
Hall, J. C., & Ramsey, L. W. 1992, AJ, 104, 1942
Henry, G. W., Fekel, F. C., & Hall D. 1995, AJ, 110, 2926
Høg, E., Fabricius, C., Makarov, V. V., et al. 2000, A&A, 355, L27
Jeffries, R. D., Bertram, D., & Spurgeon, B. R. 1995, MNRAS, 276, 397
Kalimeris, A., Mitrou, C. K., Doyle, J. G., Antonopoulou, E., & Rovithis-Livaniou, H. 1995, A&A, 293, 371
Lanza, A. F. 2005, MNRAS, 364, 238
Lanza, A. F. 2006, MNRAS, 369, 1773
Lanza, A. F., & Rodonó, M. 1999, A&A, 349, 887
Lanza, A. F., Rodono, M., & Rosner, R. 1998, MNRAS, 296, 893
López-Santiago, J., Montes, D., Fernández-Figueroa, M. J., & Ramsey, L. W. 2003, A&A, 411, 489
Matese, J. J., & Whirtmere, D. P. 1983, A&A, 117, L7
Mason, K. O., Hassall, B. J. M., Bromage, G. E., et al. 1995, MNRAS, 274, 1194
Montes, D., Fernández-Figueroa, M. J., De Castro, E., & Cornide, M. 1995, A&A, 294, 165
Montes, D., Fernández-Figueroa, M. J., De Castro, E., & Sanz-Forcada, J. 1997, A&AS, 125, 263 (Paper I)
Montes, D., Sanz-Forcada, J., Fernández-Figueroa, M. J., De Castro, E., & Poncet, A. 1998, A&A, 330, 155 (Paper II)
Montes, D., Fernández-Figueroa, M. J., De Castro, E., et al. 2000, A&AS, 146, 103 (Paper III)
Montes, D., López-Santiago, J., Gálvez, M. C., et al. 2001a, MNRAS, 328, 45
Montes, D., López-Santiago, J., Fernández-Figueroa, M. J., & Gálvez, M. C. 2001b, A&A, 379, 976
Pfeiffer, M. J., Frank, C., Baumueller, D., et al. 1998, A&AS, 130, 381
Press, W. H., Flannery, B. P., & Teukolsky, S. A. 1986, Numerical recipes. The art of scientific computing, (Cambridge: University Press)
Schmidt-Kaler, T. 1982, in Landolt-Börnstein, Vol. 2b, ed K. Schaifers, & H. H. Voig (Heidelberg: Springer)
Soderblom, D. R., Oey, M. S., Johnson, D. R. H., & Stone, R. P. S. 1990, AJ, 99, 595
Sowell, J. R., Hughes, S. B., Hall, D. S., & Howard, B. A. 2001, AJ, 122, 1965
Strassmeier, K. G., Washuettl, A., Granzer, Th., Scheck, M., & Weber, M. 2000, A&AS, 142, 275
Tonry, J., & Davis, M. 1979, AJ, 84 1511
Tonry, J., & Davis, M. 1981, AJ, 246, 666

Online Material

Table 7. *EW* of chromospheric activity indicators.

		EW(Å) in the subtracted spectra									
Obs.	φ	Ca II							Ca II IRT		
Idt.[5]		K	H	Hϵ	Hδ	Hγ	Hβ	Hα Hα_i(P+S)	λ8498	λ8542	λ8662
(1)	0.75	–	–	–	–	–	–	0.89/2.45 2.66	0.35/0.23	0.53/0.41	0.48/0.28
(1)	0.06	–	–	–	–	–	–	3.64[1] 3.27	0.63[1]	1.02[1]	0.77[1]
(1)	0.37	–	–	–	–	–	–	1.54/2.93 3.31	0.58[1]	1.18[1]	0.55[1]
(1)	0.67	–	–	–	–	–	–	1.24/2.02 2.43	–	–	–
(1)	0.98	–	–	–	–	–	–	3.52[1] 2.96	0.54[1]	0.88[1]	0.66[1]
(1)	0.30	–	–	–	–	–	–	1.43/2.21 2.88	0.38/0.22	0.60/0.43	0.48/0.27
(1)	0.60	–	–	–	–	–	–	0.90/2.31 2.47	0.43/0.10	0.80[1]	0.53/0.28
(1)	0.90	–	–	–	–	–	–	1.00/2.15 2.62	[3]	[3]	[3]
(1)	0.21	–	–	–	–	–	–	1.25/2.19 2.70	0.37/0.23	0.70/0.56	0.42/0.31
(1)	0.55	–	–	–	–	–	–	1.25/1.93 3.07	0.57[1]	0.94[1]	0.53[1]
(2)	0.74	–	–	–	–	–	0.31/0.23	1.95/2.73 4.90	–	0.71/0.32	0.58/0.32
(2)	0.07	–	–	–	–	–	0.59[1]	3.42[1] 2.93	–	1.07[1]	0.93[1]
(2)	0.47	–	–	–	–	–	0.65[1]	3.53 [1] 3.38	–	1.16 [1]	1.03[1]
(2)	0.30	–	–	–	–	–	0.88[1]	1.62/3.09 3.23	–	0.74/0.41	0.72/0.14
(2)	0.26	–	–	–	–	–	1.13[1]	5.20 [1] 4.03	–	1.25 [1]	1.14[1]
(2)	0.62	–	–	–	–	–	0.68[1]	3.95[1] 3.33	–	1.11[1]	0.95[1]
(2)	0.91	–	–	–	–	–	0.66[1]	2.58/1.58 3.19	–	0.68/0.30	0.59/0.43
(2)	0.26	–	–	–	–	–	0.91[1]	3.42/1.57 3.45	–	1.26[1]	1.34[1]
(3)	0.56	1.80/1.96	1.46/2.17	[3]	[3]	0.07/0.13[2]	0.46/0.34	2.15/1.99 3.70	0.80/0.60	0.55/0.43	0.67/0.42
(3)	0.86	3.42[1]	2.45[1]	0.62[1]	0.20[1]	0.26[1,2]	0.74[1,2]	3.99[1] 3.34	1.20[1]	0.93[1]	1.04[1]
(3)	0.17	1.92/1.27	1.31/0.98	0.589/[3]	0.09/0.10	0.12/0.15[2]	0.45/0.21[2]	1.33/2.01 2.91	0.91/0.38	0.63/0.22	0.73/0.32
(3)	0.50	1.88/1.81	1.53/1.11	0.41/0.07	0.10/0.11	0.07/0.16[2]	0.21/0.45[2]	1.85/1.81 3.25	0.78/0.65	0.49/0.39	0.73/0.43
(4)	0.70	1.09/0.82	1.08[4]/0.71	0.51/1.08[4]	0.13/0.14	0.15/0.15	0.36/0.34	1.34/2.20 2.81	0.57/0.25	0.75/0.42	0.66/0.29
(4)	0.26	0.92/0.85	0.95/0.92[4]	0.92[4]/1.49	[3]	0.18/0.08	0.31/0.34	1.89/1.60 2.79	0.55/0.41	0.70/0.44	0.63/0.40
(4)	0.57	3.03[1]	2.07[1]	0.24[1]	0.69[1]	0.50[1]	0.67[1]	3.45[1] 2.70	0.91[1]	1.19[1]	1.08[1]
(4)	0.62	1.40/0.71	0.94[4]/0.97	0.57/0.94[4]	[3]	[3]/0.19	0.36/0.28	1.19/2.26 2.58	0.57/0.28	0.60/0.41	0.56/0.43
(4)	0.66	[3]	[3]	[3]	[3]	0.15/0.21	0.30/0.27	1.19/2.06 2.59	0.60/0.31	0.72/0.46	0.58/0.36
(4)	0.87	3.12[1]	2.14[1]	0.21[1]	0.31[1]	0.37[1]	0.71[1]	3.47[1] 2.78	0.85[1]	1.25[1]	1.05[1]
(4)	0.91	3.04[1]	1.90[1]	0.33[1]	0.35[1]	0.24[1]	0.60[1]	3.31[1] 2.97	0.86[1]	1.16[1]	0.95[1]
(4)	0.95	[3]	1.34[1]	0.31[1]	[3]	0.20[1]	0.63[1]	3.46[1] 3.03	0.90[1]	1.15[1]	0.95[1]

Table 7. continued.

		EW(Å) in the subtracted spectra									
Obs.	φ	Ca II							Ca II IRT		
Idt.[5]		K	H	Hϵ	Hδ	Hγ	Hβ	Hα Hα_i(P+S)	λ8498	λ8542	λ8662
(4)	0.18	0.91/0.76	1.09/0.98[4]	0.98[4]/1.12	[3]	0.16/0.16	0.22/0.31	1.86/1.67 3.07	0.58/0.40	0.70/0.49	0.68/0.38
(4)	0.22	1.52/1.37	1.33/0.99[4]	0.99[4]/1.70	0.16/0.24	0.17/0.29	0.27/0.31	2.09/1.59 3.19	0.59/0.41	0.80/0.53	0.69/0.43
(4)	0.27	1.25/1.24	1.08/0.96[4]	0.96[4]/0.36	0.17/0.15	0.18/0.23	0.31/0.30	1.99/1.74 3.10	0.57/0.42	0.75/0.53	0.64/0.43
(4)	0.48	3.30[1]	1.97[1]	0.44[1]	0.50[1]	0.29[1]	0.67[1]	3.41[1] 2.91	0.94[1]	1.28[1]	1.12[1]
(4)	0.56	2.67[1]	2.22[1]	0.28[1]	0.36[1]	0.44[1]	0.70[1]	3.55[1] 2.91	0.99[1]	1.36[1]	1.18[1]
(5)	0.29	1.33/1.20	0.77/1.66[4]	1.66[4]	[3]	[3]	0.26/0.26	2.04/1.56 3.16	–	0.91/0.43	0.34/0.46
(5)	0.27	1.16/1.02	0.54/0.66[4]	0.66[4]	[3]	[3]	0.36/0.28	1.88/0.59 2.87	–	0.60/0.64	0.51/0.40
(5)	0.64	1.09/0.59	0.89[4]/0.81	[4]/0.35	[3]	[3]	0.30/0.24	2.05 2.87	–	0.65/0.26	0.52/0.22
(5)	0.21	0.18/1.00	1.10/0.96[4]	[4]/0.48	0.51[1]	0.14/0.11	0.41/0.21	1.89/1.83 3.19	–	0.59/0.42	0.58/0.40

Hα_i: The integrated total Hα EWs value of both components.; [1] Data for primary and secondary components not deblended.; [2] Mean value of two apertures in each spectrum or higher S/N aperture measure; [3] Data not measured due to very low S/N; [4] These are the blended value of H line of one component with Hϵ line from the other component; [5] Observing run identification (see Sect. 2).

Table 8. Emission fluxes.

	log F_S									
Obs.	Ca II							Ca II IRT		
Idt.^{5}	K	H	Hϵ	Hδ	Hγ	Hβ	Hα	λ8498	λ8542	λ8662
(1)	–	–	–	–	–	–	6.89/7.28	6.41/6.13	6.59/6.38	6.55/6.22
(1)	–	–	–	–	–	–	7.50^1	6.67^1	6.88^1	6.76^1
(1)	–	–	–	–	–	–	7.13/7.36	6.63/6.54	6.94/6.84	6.61/6.51
(1)	–	–	–	–	–	–	7.04/7.20	–	–	–
(1)	–	–	–	–	–	–	7.49^1	6.60^1	6.81^1	6.69^1
(1)	–	–	–	–	–	–	7.10/7.24	6.45/6.11	6.65/6.41	6.55/6.20
(1)	–	–	–	–	–	–	6.90/7.25	6.50/6.77	6.77/6.67	6.59/6.22
(1)	–	–	–	–	–	–	6.94/7.22	^{3}	^{3}	^{3}
(1)	–	–	–	–	–	–	7.04/7.23	6.44/6.13	6.72/6.52	6.49/6.26
(1)	–	–	–	–	–	–	7.04/7.58	6.63^1	6.84^1	6.59^1
(2)	–	–	–	–	–	6.40/6.20	7.23/7.33	–	6.72/6.28	6.63/6.28
(2)	–	–	–	–	–	6.68^1	7.48^1	–	6.90^1	6.84^1
(2)	–	–	–	–	–	6.85^1	7.15/7.38	–	6.74/6.38	6.73/5.92
(2)	–	–	–	–	–	6.72^1	7.49^1	–	6.93^1	6.88^1
(2)	–	–	–	–	–	6.74^1	7.54^1	–	6.92^1	6.85^1
(2)	–	–	–	–	–	6.96^1	7.66^1	–	6.97^1	6.93^1
(2)	–	–	–	–	–	6.73^1	7.35/7.09	–	6.70/6.25	6.64/6.41
(2)	–	–	–	–	–	6.86^1	7.48/7.09	–	6.97/6.87	7.00/6.90
(3)	7.15/7.09	7.06/7.13	^{3}	^{3}	5.73/5.94	6.57/6.38	7.28/7.19	6.77/6.55	6.61/6 .40	6.70/6.40
(3)	7.43^1	7.28^1	6.69^1	6.17^1	6.30^1	6.77^1	7.54^1	6.9 5^1	6.84^1	6.89^1
(3)	7.18/6.90	7.01/6.79	6.67/^{3}	5.83/5.82	5.96/6.00	6.56/6.16	7.07/7.19	6.83/6.35	6.67/6.11	6.73/6.28
(3)	7.17/7.06	7.08/6.84	6.51/5.64	5.87/5.86	5.73/6.03	6.23/6.49	7.21/7.15	6.76/6.58	6.56/6.36	6.73/6.41
(4)	6.93/6.71	6.93/6.65	6.60/^{3}	5.99/5.96	6.06/6.00	6.46/6.37	7.07/7.23	6.63/6.17	6.75/6.40	6.69/6.23
(4)	6.86/6.73	6.87/6.76	^{3}/6.97	^{3}	6.14/5.73	6.40/6.37	7.22/7.10	6.61/6.38	6 .72/6.42	6.67/6.37
(4)	7.38^1	7.21^1	6.28^1	6.71^1	6.58^1	6.73^1	7.48^1	6.83^1	6.95^1	6.90^1
(4)	7.04/6.65	6.872/6.79	6.65/^{3}	^{3}	^{3}/6.10	6.46/6.28	7.02/7.25	6.63/6.22	6.65/6.38	6.62/6.41
(4)	^{3}	^{3}	^{3}	^{3}	6.06/6.15	6.38/6.27	7.02/7.20	6.65/6.26	6.73/6.43	6.63/6.33
(4)	7.39^1	7.23^1	6.22^1	6.37^1	6.45^1	6.76^1	7.48^1	6.80^1	6.97^1	6.89^1
(4)	7.38^1	7.17^1	6.41^1	6.42^1	6.26^1	6.68^1	7.46^1	6.80^1	6.93^1	6.85^1
(4)	^{3}	7.02^1	6.39^1	^{3}	6.18^1	6.70^1	7.48^1	6.82^1	6.93^1	6.85^1
(4)	6.85/6.68	6.93/6.79^4	^{3}/6.85	^{3}	6.09/6.03	6.25/6.33	7.21/7.11	6.63/6.37	6.72/6.46	6.70/6.35
(4)	7.08/6.94	7.02/6.79^4	^{3}/7.03	6.08/6.20	6.11/6.29	6.34/6.33	7.26/7.09	6.64/6.38	6.77/6.50	6.71/6.41
(4)	6.99/6.89	6.93/6.78^4	^{3}/6.35	6.10/5.99	6.14/6.18	6.40/6.31	7.24/7.13	6.62/6.40	6.75/6.50	6.68/6.41
(4)	7.41^1	7.19^1	6.54^1	6.57^1	6.35^1	6.73^1	7.48^1	6.84^1	6.98^1	6.92^1
(4)	7.32^1	7.24^1	6.34^1	6.43^1	6.53^1	6.75^1	7.49^1	6.87^1	7.00^1	6.94^1
(5)	6.78/7.02	7.02/6.88^4	7.12/7.02	^{3}/^{3}	^{3}/^{3}	6.32/6.25	7.25/7.08	–	6.83/6.41	6.40/6.43
(5)	6.63/6.62	6.96/6.81^4	6.71/^{3}	^{3}/^{3}	^{3}/^{3}	6.46/6.28	7.22/6.66	–	6.65/6.58	6.58/6.37
(5)	6.84/6.71	6.93^4/6.57	^{4}/6.34	^{3}/^{3}	^{3}/^{3}	6.38/6.21	7.00/7.20	–	6.68/6.19	6.59/6.11
(5)	6.94/6.78	6.15/6.80^4	6.90/6.48	6.58^1	6.03/5.86	6.52/6.16	7.22/7.15	–	6.49/6.40	6.63/6.37

Notes as in previous table.